Topography-Dependent Effective Contact Line in Droplet Depinning

Youhua Jiang,[1] Yujin Sun,[2,3] Jaroslaw W. Drelich,[2] and Chang-Hwan Choi[1,*]
[1]Department of Mechanical Engineering, Stevens Institute of Technology, Hoboken, New Jersey 07030, USA
[2]Department of Materials Science and Engineering, Michigan Technological University, Houghton, Michigan 49931, USA
[3]School of Chemical Engineering and Technology, China University of Mining & Technology, Xuzhou 221116, People's Republic of China

(Received 20 April 2020; accepted 28 September 2020; published 27 October 2020)

The mobility of a fakir state droplet on a structured surface is fundamentally determined by the effective length of a microscopic contact line. However, it is largely unknown how the surface topography determines the effective contact line length. Based on the direct measurement of droplet adhesion force and the visualization of contact line, this work shows that effective contact line length is topography dependent as opposed to prior notion. On pored surfaces, contact line is not distorted, and the effective length approaches the droplet apparent perimeter regardless of pore dimensions. On pillared surfaces, the distortion of contact line is significantly dependent on the packing density of the pillar structures so that the effective length is as small as a pillar diameter on densely packed pillars and as large as a pillar perimeter on sparsely-packed pillars, while changing linearly between the two extremes.

DOI: 10.1103/PhysRevLett.125.184502

Placing, moving, and removing liquid droplets with controllable driving forces are crucial in many applications such as condensation, droplet manipulation, water harvesting, self-cleaning and anti-icing surfaces, and coatings [1–6]. Thus, it is important to understand how the force required to depin a droplet on a surface is dictated by the surface topography. The droplet depinning force is fundamentally governed by the shape and length of a contact line at the droplet perimeter. Especially, for a fakir droplet on a structured surface where a liquid-gas interface is suspended by partially wetted solid structures (Cassie-Baxter state), the depinning force originates from the energy consumed by the displacement of a contact line on a solid structure and the energy stored at the distorted liquid-gas interface between adjacent solid structures [7–9]. Because of the difficulty in visualizing their microscopic dynamics, the effective length of the contact line that contributes to the depinning force has been proposed and used in analyzing the droplet dynamics [9–15]. Despite its importance, how the topography of a structured surface determines the effective contact line length remains largely unknown and its estimation remains mystifying.

The depinning force results from the distortion of the liquid-gas interface which can be regarded as a stretched spring (see Fig. S1 in the Supplemental Material [16]). The spring force is proportional to the length of the anchored contact line that is surrounded by the distorted interfaces [7]. In one extreme case where the perimeter of the structure remains fully wetted during the distortion, the full perimeter (maximum) can be taken as an effective contact line length [10,15,17]. In the other extreme case where only the displacement of the contact line consumes energy with no distortion of the liquid-gas interface, the size (diameter or width) of the structure (minimum) is equivalent to the effective contact line [12,18,19]. Or, the interface distortion and contact line displacement can coexist and an effective contact line is then an arbitrary value between the structure size and perimeter [20,21]. Despite the disparity and ambiguity in the effective contact line length, all prior studies considered the ratio (x) of an effective contact line length on an individual structure (l_i) to the structural size (d) to remain constant (i.e., $l_i \propto xd$, where x is fixed), regardless of the structural dimensions or spatial distributions. This means that the contact line dynamics should be indifferent to the surface topography, which is quite questionable and needs verification. However, the dependency of an effective contact line length on surface topography has not been investigated for structured surfaces with systematically regulated contact line continuity (e.g., pillared vs pored surfaces; a contact line is discontinuous on pillared surfaces whereas it is continuous on pores surfaces) and packing density (d/λ, where λ is a periodicity of the structures).

The estimation of an effective contact line length can be accomplished by measuring droplet-surface interactive forces. Four different approaches have been used in measuring the interactive forces, including tilting [22], centrifugally rotating [23], tangential shearing [14,24,25], and vertical detaching [17,20,26–32]. The forces measured by the first three approaches are defined as the retention or lateral adhesion force, where the contact line is anisotropic along the droplet perimeter since one side is advancing (wetting) while the other is receding (dewetting). Because of the anisotropy, it is not appropriate to directly correlate

the measured force to the effective contact line length. In contrast, the fourth approach allows the contact line to be isotropic, where the contact line recedes uniformly towards the droplet center, being the most suitable one for the investigation of the effects of the surface topography on the effective contact line length. However, such an attempt has not been made yet, leaving the understanding unclear.

Here, we employ the vertical detaching approach to unveil the effects of surface topography on the effective contact line length and establish the predictive correlation model. The maximum forces required to vertically detach a fakir droplet from both micropillared (discontinuous contact line) and micropored (continuous contact line) surfaces are directly measured using a tensiometer. The correlation between the effective contact line length and structural dimensions is established by comparing the experimentally measured adhesion forces to theoretical ones, which is further verified by the visualization of the contact line dynamics.

The microstructured hydrophobic surfaces were prepared using a soft lithography technique with polydimethylsiloxane (PDMS) (see Supplemental Material [16] for details) [10,29]. The diameter (d) of the structures varied from 2.5 to 50 μm and the center-to-center pitch (λ) from 10 to 100 μm [Fig. 1(a); see also Table S1 and Figs. S2-S3 [16]]. The solid area fraction (Φ) of the surfaces ranges from 0.03 to 0.65 for pillars and 0.35 to 0.99 for pores, defined as $\pi d^2/4\lambda^2$ and $1-\pi d^2/4\lambda^2$, respectively. A smooth PDMS surface was also prepared and tested as a control, whose Φ is 1.

The measurement of the adhesion force of a water droplet (~3 μL) to the prepared surfaces of PDMS was conducted as shown in Fig. 1(b) (see Supplemental Material [16] for details) [20,27–29]. As illustrated in Fig. 1(c), the adhesion force initially increased while the stage was moving downwards, until a maximum value (referred to as a maximum adhesion force, $F_{\max}$) was reached. Then, the force decreased until the droplet was detached. The contact angle and the contact radius of a droplet were measured based on the captured image of the droplet profile using ImageJ software. The contact angle and the contact radius at $F_{\max}$ are denoted as θ_{ms} and R, respectively (see Table S2 [16]). All the experimental values were the average of at least five reproducible tests. The $F_{\max}$ represents the adhesion force at the most stable droplet shape (the most stable contact angle) in contact with the solid during depinning, depending on the dimensions of solid structures [28,33].

Figure 2 shows $F_{\max}$ with respect to Φ of the prepared surfaces. Although $F_{\max}$ generally increases with Φ, no universal dependence of $F_{\max}$ on Φ was identified. This puzzling trend cannot be explained by the contact angle hysteresis, which has been conventionally employed to quantify the droplet retention. Both $F_{\max}$ and contact angle hysteresis are essentially determined by the dynamics of

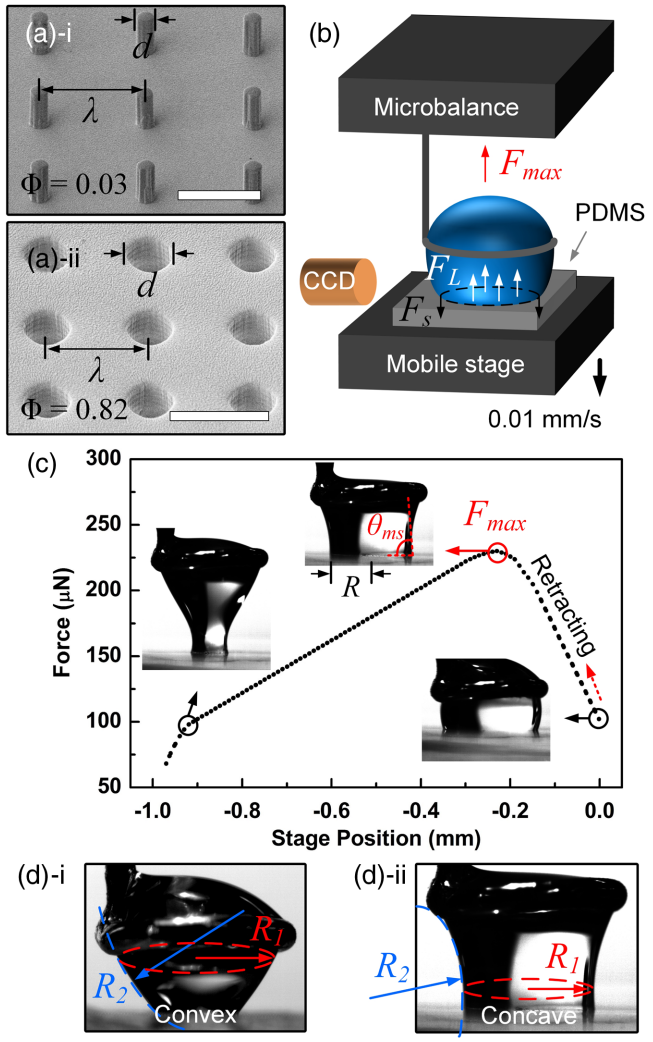

FIG. 1. (a) Scanning electron microscope images of pillared (i) and pored (ii) surfaces with varying dimensions, where λ, d, and Φ represent the structure pitch, diameter, and solid fraction, respectively. The scale bar is 20 μm. (b) Schematic of the measurement of adhesion force of a water droplet (~3 μL) on a solid surface. (c) Force measured with respect to the vertical position of a pored surface of $\Phi = 0.65$. Insets illustrate the change in the droplet shape and the maximum adhesion force is denoted as $F_{\max}$. (d) The principal radii of curvatures measured on droplets in convex and concave shapes.

contact line and its effective length. The maximum adhesion force consists of surface tension force (F_S) and Laplace pressure force (F_L), as [34–36]

$$F_{\max} = \gamma \sum_{i=1}^{n} l_i \sin\theta_i - A\Delta P, \tag{1}$$

where γ is the surface tension of water, n is the number of structures along the droplet perimeter, l_i is the length of the effective contact line segment per each structure with a contact angle of θ_i, A is the droplet base area, and ΔP is the Laplace pressure. ΔP is estimated by droplet surface

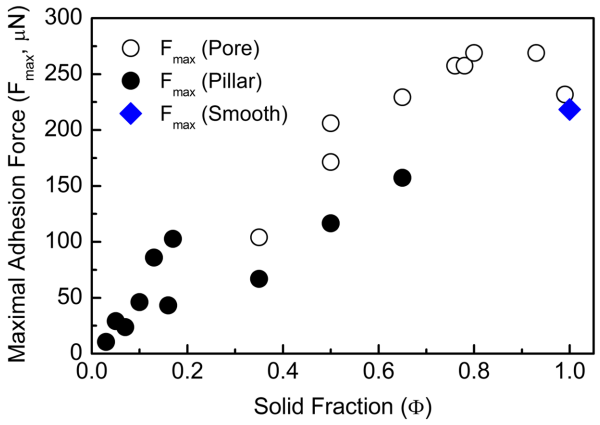

FIG. 2. Measured maximum adhesion forces ($F_{\max}$) on pillared (filled circle), pored (circle), and smooth (filled diamond) surfaces with respect to solid fractions (Φ).

curvatures [Fig. 1(d)], as $\Delta P = \gamma\,(1/R_1 + 1/R_2)$, where R_2 is a negative value for concave droplet shape. A positive ΔP represents a force to maintain a spherical droplet shape, and hence F_L works against F_S. At the most stable state, the droplet is axisymmetric with an apparently circular base ($A = \pi R^2$) and the contact angles are identical everywhere along the droplet perimeter. $F_{\max}$ can be simplified as [28,33]

$$F_{\max} = \gamma 2\pi R\delta \sin\theta_{ms} - \pi R^2 \Delta P, \tag{2}$$

where $2\pi R\delta$ represents the effective contact line length along the apparent droplet perimeter ($2\pi R$). Or, δ represents the ratio of the effective contact line length to the apparent perimeter (effective contact line fraction) [10]. Since the contact line is isotropic, $2\pi R\delta = nl_i$, and the apparent droplet perimeter equals the summation of the total number of pitches along the perimeter ($2\pi R \approx n\lambda$) [10], and hence,

$$\delta = \frac{l_i}{\lambda} = \frac{xd}{\lambda}, \tag{3}$$

where x can be as large as π, if the unit effective contact line length (l_i) equals the perimeter of the unit structure. On an ideally smooth surface, δ is unity.

Based on Eq. (2), δ can experimentally be estimated as

$$\delta = \frac{F_{\max} + \pi R^2 \Delta P}{\gamma 2\pi R \sin\theta_{ms}}. \tag{4}$$

Figure 3(a) shows the δ values with respect to Φ, computed according to Eq. (4) (see Table S2 for the experimental data [16]). For droplets on pored surfaces, δ remain practically constant ($\delta \approx 1$) irrespective of the structural dimensions. This indicates that the contact line cannot effectively distort in recession on pored surfaces and the effective contact line is equivalent to the apparent droplet perimeter ($2\pi R$). It is corroborated by the

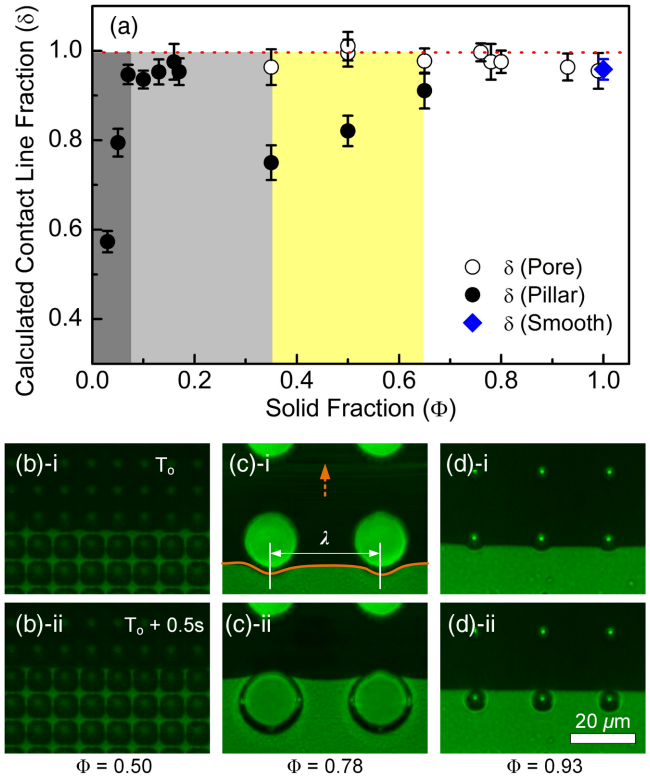

FIG. 3. (a) The calculated contact line fraction (δ) on pillared (filled circle), pored (circle), and smooth (filled diamond) surfaces with respect to solid fractions (Φ). The red-dotted line at $\delta = 1$ is for the guide for reading. The dark-gray, light-gray, and yellow regimes show three distinct trends of δ on pillared surfaces (filled circle) with respect to Φ. (b)–(d) The shapes of the pinned contact line on the pored surfaces (orange-solid line) of Φ = 0.50, 0.78, and 0.93, respectively, on the brink of detachment (i) and right after the detachment (ii).

visualization of the contact line using a reflective interference contrast microscopy (see Supplemental Material [16]) [10], as shown in Figs. 3(b)–3(d), where δ is effectively the maximally distorted contact line (orange-solid line) divided by the pitch (λ). This agrees with the previous studies showing that receding contact angles [9,37] and measured adhesion force [27] on pored surfaces remain roughly constant despite the variations in structural dimensions. Although the visualizations were conducted independently using a receding droplet with reducing volume, the visualized dynamics of the contact line represented those at the most stable state, because they both were measured in the constant contact angle modes as a droplet boundary continuously recedes (see Fig. S4 [16]). In contrast, for droplets on pillared surfaces, δ varies significantly with Φ. The distinct behavior of δ on pillared surfaces mainly results from the discontinuity of the contact line (i.e., the contact line is isolated on each pillar tip surrounded by suspended liquid-gas interface), whereas that on pored surface is continuous. Although δ does not show the global dependence on Φ of pillared surfaces, Fig. 3(a) shows

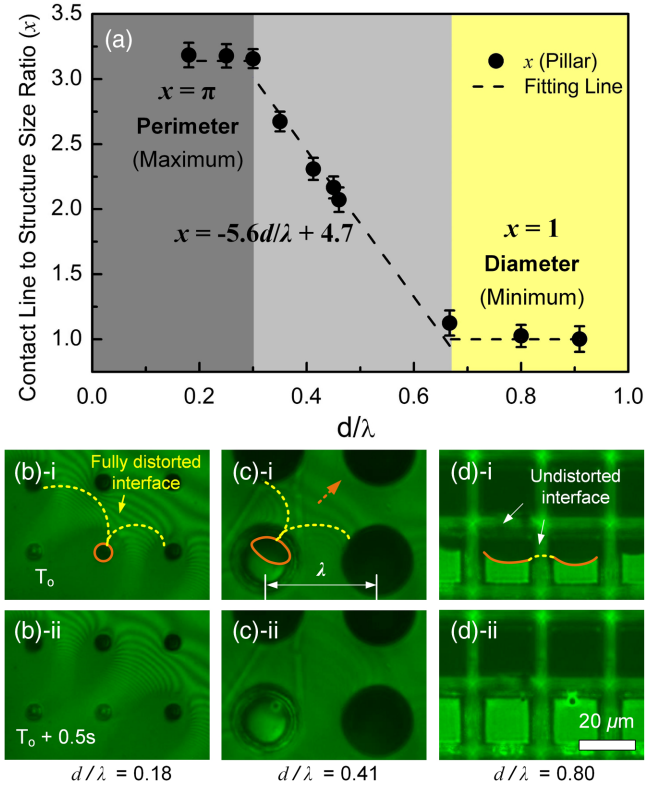

FIG. 4. (a) The ratio (x) of the effective contact line length (l_i) on a pillar to a pillar size (d) with respect to the packing density (d/λ) of pillars. The black-dashed line represents the best fitting line. (b)–(d) The effective contact lines on pillar tops (orange-solid lines) and the lowest local positions of the distorted liquid-gas interfaces in between pillars (yellow-dotted line) in the cases of $d/\lambda = 0.18$, 0.41, and 0.80, respectively, on the brink of detachment (i) and right after the detachment (ii).

distinct trends of δ within the three local regimes of Φ as marked in different colors.

Further noting that the contact line dynamics can be distinct depending on the packing density (d/λ) of pillar structures [9], the ratio of the unit effective contact line length to a pillar diameter ($x = l_i/d = \delta\lambda/d$) is plotted with respect to d/λ in Fig. 4(a). It shows three distinctive regimes as follows. For sparsely packed pillars ($d/\lambda < 0.3$), $x \cong \pi$. It is the maximum value for the effective contact line (l_i) to reach on a circular pillar top, suggesting that the effective contact line follows almost the full perimeter of the circular pillar top in the case of sparsely packed pillars. This is because the sparsely packed pillars allow the liquid-gas interface to be fully distorted in the vicinity of the wetted pillars (dark regions), as shown in Fig. 4(b) where the distorted liquid-gas interface (dark-bright interference fringes) surrounds the entire wetted pillar top (orange-solid line) right before detachment. The yellow-dotted lines in Fig. 4(b) represent the lowest local positions of the distorted interface [9], which forms a continuous interface with the liquid remained on the pillar top (farthest edge of the dark regions). Their distance represents the extent of distortion, and the contact line between them is the effective contact line (see Fig. S1 [16]). In this case, the liquid-gas interface consumes much energy in distortion and the entire pillar top perimeter effectively contributes to $F_{\max}$. In contrast, for densely packed pillars ($d/\lambda > 0.67$), $x \cong 1$, indicating that the effective contact line length (l_i) roughly equals the pillar size (d). This is because the liquid-gas interface cannot distort much in such a confined space relative to a large pillar size, as shown in Fig. 4(d) where the interference fringes are not found around the pillars. In this case, the consumption of energy and contribution to $F_{\max}$ by the distortion of liquid-gas interface are small. Thus, the displacement of the contact line starts relatively early and mainly contributes to $F_{\max}$, limiting the effective contact line length not to exceed the pillar size. For moderately packed pillars ($0.3 \leq d/\lambda \leq 0.67$) between the two extremes, x decreases almost linearly from $\sim\pi$ to ~ 1 with the increase in d/λ. In this regime, the contact line starts to recede on the pillar top along with the distortion of the liquid-gas interface, as shown in Fig. 4(c) where the orange-solid line represents the effective contact line. This is because the distortion of the liquid-gas interface accompanies a decrease in the local (microscopic) contact angle on a pillar top, and the local contact line recedes when the contact angle reaches the intrinsic receding contact angle of the pillar top surface. Thus, the effective contact line length contributing to $F_{\max}$ is smaller than the full pillar perimeter (πd) but greater than the pillar diameter (d). Such a behavior becomes more pronounced on the pillared surface with a greater value of d/λ.

Based on the results, the empirical dependence of x on d/λ can be summarized as

$$x = \begin{cases} \pi, & d/\lambda < 0.3 \\ -5.6d/\lambda + 4.7, & 0.3 \leq d/\lambda \leq 0.67 \\ 1, & d/\lambda > 0.67 \end{cases}. \quad (5)$$

This empirical correlation also supports the experimental data reported by others. For example, Paxson and Varanasi measured the adhesion force of a water droplet on pillared surfaces and found that the increase rate of the adhesion force with d/λ was retarded when the value of d/λ reached 0.375 [17]. The result implies that the effective contact line length on the pillared surface, i.e., the value of x, would start to decrease when the packing density of the pillars increased greater than the value of 0.375. Meanwhile, the empirical correlation obtained in this study may need modifications depending on other factors such as the direction and velocity of a droplet motion, droplet size, liquid property (e.g., surface tension), intrinsic hydrophobicity of solid structures, and the shape, edge roughness, and curvature of a solid structure [8,14,24,27,35,38–40]. Nonetheless, the main discovery made in this work that the effective contact line length differs depending on the continuity of the contact line and structural packing density should universally hold true. In other words, the common

notion of the invariable ratio of the effective contact line length to the structure size regardless of a packing density, suggested by or adopted in many previous studies [7,10,12,15,17–19,21] should not be taken for granted but applied with great care, since the variation of the effective contact line length can be as large as π times.

In conclusions, this study shows how the effective contact line length, which essentially determines the droplet mobility, depends on surface topography, enabled by the direct measurement of the droplet maximum adhesion force and the visualization of the microscopic contact line dynamics. As opposed to most studies dealing with contact line, results here reveal that the effective contact line length on a structured surface cannot be considered as a constant but varies distinctly with respect to the structure type and dimensions. On pored surfaces (continuous contact line), the contact line is not significantly distorted at the most stable state and the effective contact line length equals the apparent perimeter of the droplet boundary despite the variation in the structural dimensions. In contrast, on pillared surfaces (discontinuous contact line), the effective contact line length significantly varies with respect to the packing density (i.e., the pillar size-to-pitch ratio) of the structure. On sparsely packed pillars, the effective length reaches the maximum as pillar top perimeter. As the packing density increases to the first critical value (∼0.3), the effective length starts to decrease linearly. As the packing density increases to the second critical value (∼0.67), the effective length reaches the minimum as pillar diameter. The novel insights of the topography-dependent effective contact line length on structured hydrophobic surfaces are of great significance in the fundamental understanding of the droplet dynamics and the proper design of the surfaces for tailored droplet retention.

This work has been supported in part by National Science Foundation Grants (No. ECCS-1202269 and No. CMMI-1462499). The authors declare no competing financial interest.

*To whom correspondence should be addressed.
cchoi@stevens.edu

[1] J. B. Boreyko and C.-H. Chen, Self-Propelled Dropwise Condensate on Superhydrophobic Surfaces, Phys. Rev. Lett. **103**, 184501 (2009).

[2] N. Miljkovic, R. Enright, Y. Nam, K. Lopez, N. Dou, J. Sack, and E. N. Wang, Jumping-droplet-enhanced condensation on scalable superhydrophobic nanostructured surfaces, Nano Lett. **13**, 179 (2013).

[3] C. Neinhuis and W. Barthlott, Characterization and distribution of water-repellent, self-cleaning plant surfaces, Ann. Bot. **79**, 667 (1997).

[4] V. Bahadur, L. Mishchenko, B. Hatton, J. A. Taylor, J. Aizenberg, and T. Krupenkin, Predictive model for ice formation on superhydrophobic surfaces, Langmuir **27**, 14143 (2011).

[5] Y. Jiang, C. Machado, S. Savarirayan, N. A. Patankar, and K.-C. Park, Onset time of fog collection, Soft Matter **15**, 6779 (2019).

[6] J. Drelich and A. Marmur, Physics and applications of superhydrophobic and superhydrophilic surfaces and coatings, Surf. Innov. **2**, 211 (2014).

[7] M. Reyssat and D. Quéré, Contact angle hysteresis generated by strong dilute defects, J. Phys. Chem. B **113**, 3906 (2009).

[8] H. J. Butt, N. Gao, P. Papadopoulos, W. Steffen, M. Kappl, and R. Berger, Energy dissipation of moving drops on superhydrophobic and superoleophobic surfaces, Langmuir **33**, 107 (2017).

[9] Y. Jiang, W. Xu, M. A. Sarshar, and C.-H. Choi, Generalized models for advancing and receding contact angles of fakir droplets on pillared and pored surfaces, J. Colloid Interface Sci. **552**, 359 (2019).

[10] W. Xu and C. H. Choi, From sticky to Slippery Droplets: Dynamics of Contact Line Depinning on Superhydrophobic Surfaces, Phys. Rev. Lett. **109**, 024504 (2012).

[11] L. Gao and T. J. McCarthy, Teflon is hydrophilic. Comments on definitions of hydrophobic, shear versus tensile hydrophobicity, and wettability characterization, Langmuir **24**, 9183 (2008).

[12] W. Choi, A. Tuteja, J. M. Mabry, R. E. Cohen, and G. H. McKinley, A modified Cassie-Baxter relationship to explain contact angle hysteresis and anisotropy on non-wetting textured surfaces, J. Colloid Interface Sci. **339**, 208 (2009).

[13] D. Öner and T. J. McCarthy, Ultrahydrophobic surfaces. Effects of topography length scales on wettability, Langmuir **16**, 7777 (2000).

[14] S. Qiao, S. Li, Q. Li, B. Li, K. Liu, and X. Q. Feng, Friction of droplets sliding on microstructured superhydrophobic surfaces, Langmuir **33**, 13480 (2017).

[15] C. W. Extrand and S. I. Moon, Repellency of the lotus leaf: contact angles, drop retention, and sliding angles, Langmuir **30**, 8791 (2014).

[16] See Supplemental Material at http://link.aps.org/supplemental/10.1103/PhysRevLett.125.184502 for experimental details.

[17] A. T. Paxson and K. K. Varanasi, Self-similarity of contact line depinning from textured surfaces, Nat. Commun. **4**, 1492 (2013).

[18] S. T. Larsen and R. Taboryski, A Cassie-like law using triple phase boundary line fractions for faceted droplets on chemically heterogeneous surfaces, Langmuir **25**, 1282 (2009).

[19] P. Papadopoulos, L. Mammen, X. Deng, D. Vollmer, and H. J. Butt, How superhydrophobicity breaks down, Proc. Natl. Acad. Sci. U.S.A. **110**, 3254 (2013).

[20] Y. Sun, Y. Jiang, C.-H. Choi, G. Xie, Q. Liu, and J. W. Drelich, Direct measurements of adhesion forces of water droplets on smooth and patterned polymers, Surf. Innov. **6**, 93 (2018).

[21] R. Raj, R. Enright, Y. Zhu, S. Adera, and E. N. Wang, Unified model for contact angle hysteresis on heterogeneous and superhydrophobic surfaces, Langmuir **28**, 15777 (2012).
[22] C. Antonini, F. J. Carmona, E. Pierce, M. Marengo, and A. Amirfazli, General methodology for evaluating the adhesion force of drops and bubbles on solid surfaces, Langmuir **25**, 6143 (2009).
[23] R. Tadmor, P. Bahadur, A. Leh, H. E. N'guessan, R. Jaini, and L. Dang, Measurement of Lateral Adhesion Forces at the Interface Between a Liquid Drop and a substrate, Phys. Rev. Lett. **103**, 266101 (2009).
[24] D. W. Pilat, P. Papadopoulos, D. Schäffel, D. Vollmer, R. Berger, and H. J. Butt, Dynamic measurement of the force required to move a liquid drop on a solid surface, Langmuir **28**, 16812 (2012).
[25] N. Gao, F. Geyer, D. W. Pilat, S. Wooh, D. Vollmer, H.-J. Butt, and R. Berger, How drops start sliding over solid surfaces, Nat. Phys. **14**, 191 (2018).
[26] B. Samuel, H. Zhao, and K. Y. Law, Study of wetting and adhesion interactions between water and various polymer and superhydrophobic surfaces, J. Phys. Chem. C **115**, 14852 (2011).
[27] D. Li, Y. Xue, P. Lv, S. Huang, H. Lin, and H. Duan, Receding dynamics of contact lines and size-dependent adhesion on microstructured hydrophobic surfaces, Soft Matter **12**, 4257 (2016).
[28] Y. Sun, Y. Jiang, C.-H. Choi, G. Xie, Q. Liu, and J. W. Drelich, The most stable state of a droplet on anisotropic patterns: support for a missing link, Surf. Innov. **6**, 133 (2018).
[29] Y. Jiang, Y. Sun, J. W. Drelich, and C.-H. Choi, Spontaneous spreading of a droplet: the role of solid continuity and advancing contact angle, Langmuir **34**, 4945 (2018).
[30] D. Wang, Y. Jiang, Z. Zhu, W. Yin, K. Asawa, C.-H. Choi, and J. W. Drelich, Contact line and adhesion force of droplets on concentric ring-textured hydrophobic surfaces, Langmuir **36**, 2622 (2020).
[31] R. Tadmor, R. Das, S. Gulec, J. Liu, H. E. N'guessan, M. Shah, P. S. Wasnik, and S. B. Yadav, Solid–liquid work of adhesion, Langmuir **33**, 3594 (2017).
[32] S. Gulec, S. Yadav, R. Das, V. Bhave, and R. Tadmor, The influence of gravity on contact angle and circumference of sessile and pendant drops has a crucial historic aspect, Langmuir **35**, 5435 (2019).
[33] D. Cwickel, Y. Paz, and A. Marmur, Contact angle measurement on rough surfaces: the missing link, Surf. Innov. **5**, 190 (2017).
[34] E. J. De Souza, L. Gao, T. J. McCarthy, E. Arzt, and A. J. Crosby, Effect of contact angle hysteresis on the measurement of capillary forces, Langmuir **24**, 1391 (2008).
[35] H. J. Butt, I. V. Roisman, M. Brinkmann, P. Papadopoulos, D. Vollmer, and C. Semprebon, Characterization of super liquid-repellent surfaces, Curr. Opin. Colloid Interface Sci. **19**, 343 (2014).
[36] H. Chen, T. Tang, H. Zhao, K. Y. Law, and A. Amirfazli, How pinning and contact angle hysteresis govern quasi-static liquid drop transfer, Soft Matter **12**, 1998 (2016).
[37] E. Martines, K. Seunarine, H. Morgan, N. Gadegaard, C. D. W. Wilkinson, and M. O. Riehle, Superhydrophobicity and superhydrophilicity of regular nanopatterns, Nano Lett. **5**, 2097 (2005).
[38] H. J. Butt, C. Semprebon, P. Papadopoulos, D. Vollmer, M. Brinkmann, and M. Ciccotti, Design principles for superamphiphobic surfaces, Soft Matter **9**, 418 (2013).
[39] T.-S. Wong and C.-M. Ho, Dependence of macroscopic wetting on nanoscopic surface textures, Langmuir **25**, 12851 (2009).
[40] X. Chen, R. Ma, J. Li, C. Hao, W. Guo, B. L. Luk, S. C. Li, S. Yao, and Z. Wang, Evaporation of Droplets on Superhydrophobic Surfaces: Surface Roughness and Small Droplet Size Effects, Phys. Rev. Lett. **109**, 116101 (2012).